Spectroscopic Studies and Laser Operation of Pr,Mg:SrAl$_{12}$O$_{19}$

by Larry D. Merkle and Bahram Zandi
Army Research Laboratory

Richard Moncorgé and Yannick Guyot
Laboratoire de Physico-Chimie des Matériaux Luminescents

Horacio R. Verdun and Bruce McIntosh
Fibertek, Inc.

DTIC QUALITY INSPECTED 3

19970227 033

Army Research Laboratory

Adelphi, MD 20783-1197

ARL-TR-1228   **February 1997**

Spectroscopic Studies and Laser Operation of Pr,Mg:SrAl$_{12}$O$_{19}$

Larry D. Merkle and Bahram Zandi
Sensors and Electron Devices Directorate, ARL

Richard Moncorgé and Yannick Guyot
Laboratoire de Physico-Chimie des Matériaux Luminescents

Horacio R. Verdun and Bruce McIntosh
Fibertek, Inc.

DTIC QUALITY INSPECTED 8

Abstract

Pr^{3+}-doped $SrAl_{12}O_{19}$ has been investigated spectroscopically as a visible laser material. Its $^3P_0$ fluorescence lifetime is rather long for an oxide: about 35 µs. This excited state exhibits only mild concentration and temperature quenching, so that concentrations high enough to give good ground-state absorption into the ^3P_J manifolds still give strong, long-lived emission. Ground-state absorption into the $4f5d$ configuration begins at relatively high energy, so that excited-state absorption into this configuration is less likely to be significant at laser wavelengths in $SrAl_{12}O_{19}$ than in many other oxides, such as $Y_3Al_5O_{12}$. The stimulated emission cross sections of major emission lines have been estimated, and are quite reasonable for laser operation. Laser-pumped laser operation has been demonstrated in the red ($^3P_0 \rightarrow {}^3F_2$) at room temperature and in the blue-green ($^3P_0 \rightarrow {}^3H_4$) at cryogenic temperatures.

Contents

Figures

Tables

1. Introduction

Among rare-earth ions capable of visible laser emission, Pr^{3+} is particularly attractive because of the strong absorption transitions to and fluorescence transitions from the closely grouped $^3P_0$, $^3P_1$, $^3P_2$, and $^1I_6$ manifolds. Laser operation has been reported for several Pr-doped solids [1–6]. Two limitations of Pr^{3+} are the scarcity of excited states above $^3P_2$, making lamp pumping inefficient, and the short upper-state lifetime concomitant with the large fluorescence linestrengths, making energy storage difficult. Ongoing progress in upconversion pumping of rare-earth lasers and in wide-bandgap diode lasers raises the prospect of alleviating the pumping problem. It is therefore of interest to investigate new crystalline hosts in which Pr^{3+} may exhibit a longer $^3P_0$ fluorescence lifetime. Not surprisingly, fluorides such as $Pr:YLiF_4$ exhibit longer lifetimes than oxides such as $Pr:Y_3Al_5O_{12}$ (Pr:YAG) or $Pr:YAlO_3$ [6]. However, in view of the generally superior thermomechanical properties of oxides, it is worthwhile to seek oxide hosts that may make the $^3P_0$ lifetime longer.

We present here results of the spectroscopy of such a host for Pr^{3+}, $SrAl_{12}O_{19}$. Because this strontium aluminate crystal has the magneto-plumbite structure, we refer to it by the acronym SAM. It has space group $P6_3/mmc$, and rare-earth dopants are believed to enter the Sr site, which has point group D_{3h} [7,8]. Its three-fold axis is parallel to the crystallo-graphic c-axis, and the Sr ion's nearest neighbors are six oxygens in the a-plane containing the Sr, plus sets of three oxygen ions above and below that plane [9]. These nearest-neighbor oxygen ions are significantly farther from the cation nucleus in this site than in the Y site of YAG, suggesting that the dopant may encounter a relatively weak crystal field [7,10]. This crystal has been studied as a host for Nd^{3+}, and is very similar to $LaMgAl_{11}O_{19}$, which has proven to be a good laser material when doped with Nd^{3+} [11,12].

This report summarizes our study of the spectroscopy of Pr,Mg:SAM, portions of which have been published elsewhere [13,14]. Section 2 describes the growth of the crystals used in the study and outlines our experimental apparatus and techniques. We then present the absorption spectroscopy, fluorescence spectra, and lifetimes (sect. 3 to 5). In section 6, we analyze the absorption strength and fluorescence branching ratio data, based on the theory of Judd and Ofelt. We performed simple laser experiments at both cryogenic and room temperatures; the results of these are reported in section 7, as are estimates of the stimulated emission cross sections for the most prominent emission lines. We draw conclusions concerning the promise of this material in the final section.

2. Crystal Growth and Experiments

We doped the $SrAl_{12}O_{19}$ by codoping the starting materials with equal concentrations of Pr and Mg; this approach facilitates the introduction of the trivalent Pr into the divalent Sr site. Samples were grown with 1, 5, and 10 atomic percent (at.%) of each dopant, in terms of the stoichiometric Sr concentration. Powders of $SrCO_3$ (supplied by Cerac at 99.999-percent purity), Al_2O_3 (Cerac 99.999 percent), Pr_2O_3 (Cerac 99.9 percent), and MgO (Johnson Matthey 99.999 percent) were dried at 200°C for 12 hours in air so that any water was removed. Stoichiometric amounts were then weighed, mixed together in a ball mill, and pressed to about 15 tons with a hydraulic press. The pellets formed were 1 in. in diameter and 1/2 in. high. They were then sintered at 1400°C for 12 hours in an 80-percent Ar, 20-percent O_2 atmosphere. The resulting ceramic pellets were hard and white.

Crystals were grown by the Czochralski method in an iridium crucible 1.25 in. in diameter and 1.25 in. high. Power was supplied by a 7.5-kW Pillar rf generator, controlled by an optical pyrometer aimed at the lower half of the crucible. Ceramic pellets were placed in the crucible and melted, and the melt was allowed to homogenize for about 15 minutes. For the initial growth, a pointed iridium rod with a vertical slot at the tip was used as a seed. A piece of the crystal grown from the iridium rod was then oriented and used as the seed to grow the next crystals. The seed was rotated at 80 rpm. A growth rate of 2 mm/hr was used at first, but later crystals were grown at 3 mm/hr with similar results. The atmosphere for growth was 99-percent N_2 and 1-percent O_2.

Several crystals were grown in two orientations: (001) and (100). They were allowed to cool slowly overnight and were about 2 cm long, 1 cm in diameter, and light green. The crystals grown in the (001) direction faceted into a hexagonal shape during growth, and on cooling, they cleaved in several places perpendicular to the growth direction. Crystals grown along (100) had an elliptical cross section with facets on the sides perpendicular to the c-axis. Several cleaves also formed along the growth direction perpendicular to the c-axis. All crystals contained some precipitate. We reduced this problem somewhat by growing the crystal with 15-percent excess $SrCO_3$ by weight, but some precipitate remained. Samples were cut from the core of the crystals, which was usually free of precipitate.

Three samples have been analyzed for Pr concentration by Galbraith Laboratories in Knoxville, TN. Two were grown from melts containing 10-at.% Pr and 10-at.% Mg, and one from a melt containing 1 at.% of each dopant. The results indicate a distribution coefficient of 0.91 ± 0.05, surprisingly close to unity for a system that requires charge compensation. This must depend sensitively on ionic size, as two related host crystals, $BaAl_{12}O_{19}$ and $CaAl_{12}O_{19}$, grown from melts containing up to 8-at.% Pr and Mg, incorporated very little Pr.

In this study of Pr,Mg:SAM, we measured optical absorption and fluorescence spectra, took fluorescence lifetime data, and performed laser-pumped laser experiments, all at both cryogenic and room temperatures. Absorption spectra were taken on a Perkin-Elmer Lambda-Nine spectrophotometer. Polarized spectra were taken from 300 to 2600 nm at room temperature, and unpolarized spectra extended to 190 nm. Because of the size of the CTI cryogenic refrigerator dewar tail used for low-temperature spectroscopy, we had to remove the spectrophotometer's depolarizing and polarizing crystals; thus, at low temperatures, absorption spectra were unpolarized except between 425 and 825 nm, where a thin-sheet polarizer could be used. We took fluorescence spectra using a Spex F222 spectrometer with prism polarizers and a selection of differently blazed gratings. The signal was detected by a Hamamatsu R928 photomultiplier tube or a North Coast liquid-nitrogen-cooled Ge detector, depending on wavelength. We corrected the detection system for its dependence on wavelength and polarization using an Optronic Laboratories standard lamp traceable to NIST (National Institute of Standards and Technology) standards. Fluorescence was excited by an Xe short-arc lamp, a Laser Science Inc. nitrogen laser-pumped dye laser, or the H_2 Raman-shifted output of a Continuum dye laser pumped by a Q-switched and frequency-doubled Continuum Nd:YAG laser.

These same pulsed lasers were used as excitation sources for the fluorescence lifetime measurements. In this case, the transient fluorescence was detected by the photomultiplier tube and recorded on a Tektronix DSA 602A digitizing oscilloscope. For the laser experiments, the samples were pumped by the Raman-shifted output of the doubled-Nd:YAG-pumped dye laser using Rhodamine or by a tripled-Nd:YAG-pumped dye laser using Coumarin dye.

3. Absorption Spectroscopy

Figure 1 shows the room-temperature absorption spectra for both π and σ (electric field parallel and perpendicular to the crystalline c-axis, respectively) for a 5-percent Pr,Mg:SAM crystal. The actual Pr concentration in the sample is about 1.54×10^{20} cm^{-3}. The small step near 860 nm and the baseline drift are alignment and polarization artifacts. The σ-polarized transitions tend to be stronger than the π-polarized, probably because of the high symmetry of the D_{3h} site along the c-axis. (There is a reflection plane perpendicular to the c-axis.) The groups of peaks correspond to transitions from the $^3H_4$ manifold to the following manifolds: $^3H_6$ (about 2100–2400 nm), $^3F_2$ (1900–2000 nm), $^3F_3$ (1500–1600 nm), $^3F_4$ (1400–1500 nm), $^1G_4$ (950–1050 nm), $^1D_2$ (580–600 nm), and the closely grouped $^3P_0$, $^3P_1$, $^1I_6$, and $^3P_2$ (440–500 nm). The strong $^3F_3$ σ-polarized peak at 1554 nm has an effective cross section of at least 8×10^{-20} cm^2, large enough to be of interest for saturable absorption Q-switching [15]. Disappointingly, however, at 1530 nm, the wavelength typical of eyesafe Er:glass lasers, the cross section is much smaller, about 9×10^{-21} cm^2.

Figure 2 shows that the onset energy of strong ultraviolet (UV) absorption is substantially higher in Pr,Mg:SAM than in Pr:YAG, and somewhat higher than in Pr:Ca$_5$(PO$_4$)$_3$F. This is desirable, as this energy onset may cause the excited-state absorption transitions from $^3P_0$ to these higher states to move to short enough wavelengths not to compete with stimulated emission. Excited-state absorption at visible wavelengths is substantial in Pr:YAG [16,17].

Since it is thought that the strong UV absorption in Pr:YAG terminates on the lowest $4f5d$ energy level, we suspect the same origin for the absorption in Pr,Mg:SAM. We can test this possibility by comparing the host dependence of the peak energy with that of the energy separation between $4f^2$

Figure 1. Room-temperature polarized ground-state absorption of a Pr,Mg:SAM sample with 5-percent nominal Pr and Mg concentrations. Actual Pr concentration is about 1.54×10^{20} cm^{-3}. Baselines are offset for clarity.
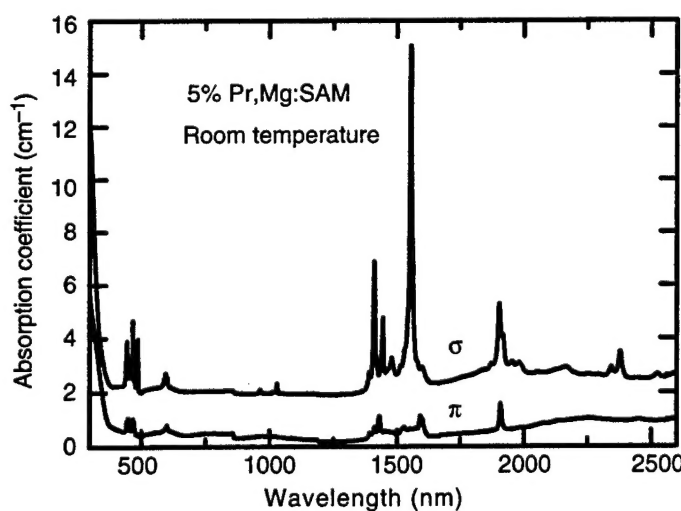
and $4f5d$ predicted by a simple model proposed by Morrison [18]. This model calculates the change in the $5d$ to $4f$ energy difference due to the polarizability of the ligands:

$$\left(E_{5d} - E_{4f}\right)_{\text{solid}} = \left(E_{5d} - E_{4f}\right)_{\text{free ion}} - \sigma_2 \Sigma_i \left(\alpha_i e^2 / R_i^6\right),$$ (1)

where α_i is the polarizability of the ith ligand and R_i is the distance between the rare earth and that ligand. The factor σ_2 is the difference in expectation value of r^2 between the $5d$ and $4f$ wave functions, and is treated as the sole adjustable parameter. Table 1 gives results for a best-fit σ_2 value of 3.10 Å^2, where $(E_{5d} - E_{4f})_{\text{free ion}} = 61,171$ cm^{-1} [19]. The variation among the hosts agrees well enough with the model results for us to assign the UV absorption to transitions from the $4f^2$ ground state to $4f5d$ states. Thus the relatively high onset energy of the UV absorption in Pr,Mg:SAM has another advantage: It should result in weaker mixing of the even-parity $5d$ wavefunctions with the odd-parity $4f$ wavefunctions, potentially yielding a relatively long $^3P_0$ fluorescence lifetime.

Figure 3 shows the σ-polarized absorption of 5-percent Pr,Mg:SAM in greater detail for the $^3P_0$, $^3P_1$, $^3P_2$, and $^1I_6$ manifolds at room temperature and 17 K. The strongest absorption peak in this region is attributable to a transition from the ground state of $^3H_4$ to a state of $^3P_1$, and the data of figure 1 indicate that the peak's effective cross section at room temperature is

Figure 2. Room-temperature unpolarized absorption spectrum of Pr,Mg:SAM compared to those of Pr:Ca$_5$(PO$_4$)$_3$F and Pr:YAG. Baselines are offset for clarity.
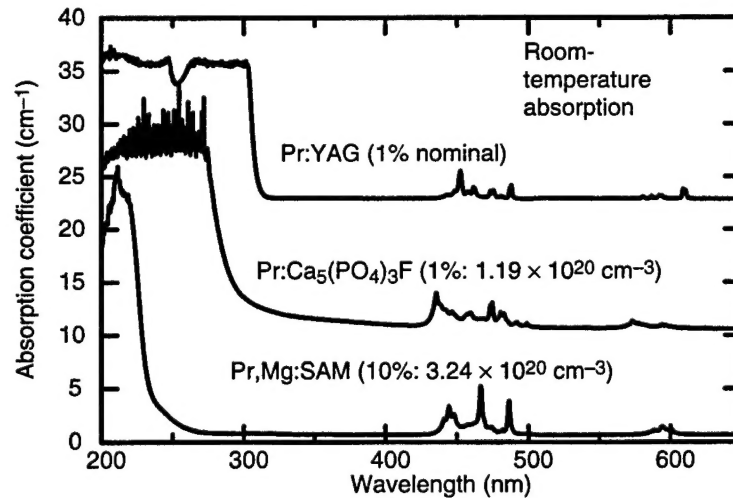
Table 1. Observed and predicted energies of lowest energy ultraviolet absorption band in three Pr-doped crystals.

Material	Observed lowest energy UV absorption band (cm^{-1})	Best-fit energy of lowest $4f^15d^1$ band (cm^{-1})
Pr:YAG	35,500	35,200
Pr:Ca$_5$(PO$_4$)$_3$F	40,000	40,900 (Ca I site)[a]
Pr,Mg:SAM	47,000	46,400

[a]For Pr in Ca II site of Ca$_5$(PO$_4$)$_3$F: 42,200 cm^{-1}.

Figure 3. Temperature dependence of σ-polarized absorption of a 4.3-mm-thick 5-percent Pr,Mg:SAM sample in region of $^3P_0$, $^3P_1$, $^3P_2$, and $^1I_6$ manifolds.
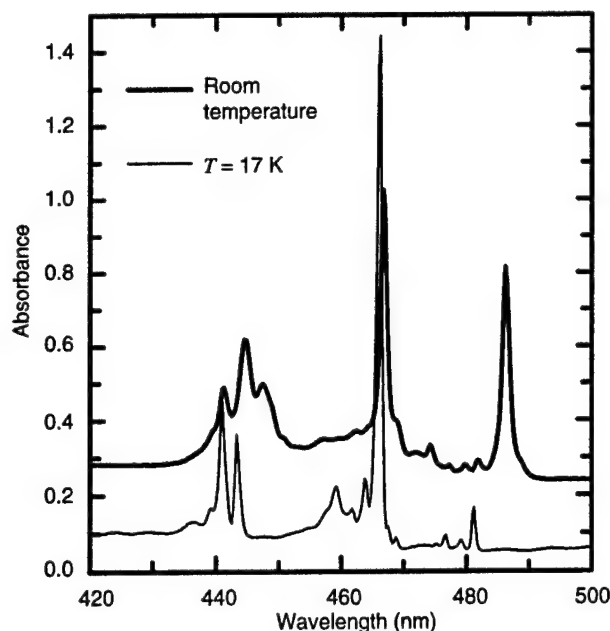
about 1.6×10^{-20} cm^2. Interestingly, the second strongest room-temperature line, at 486 nm, is absent at low temperature and thus is a "hot band." Its position and temperature-dependent strength indicate that it originates about 190 cm^{-1} above the ground state, and thus its intrinsic line strength must be rather large to yield the observed room-temperature effective cross section of 1.2×10^{-20} cm^2.

Low-temperature absorption data have been used to locate some of the relevant excited states in Pr,Mg:SAM. This process is somewhat complicated by the weakness of many of the transitions in 1-percent Pr,Mg:SAM and by the likelihood of Pr-Pr interactions in the more heavily doped samples. Also, the Mg charge compensators may give rise to perturbed sites at all concentrations. Nevertheless, some transitions can be discerned, and their overall pattern is satisfactorily consistent with the selection rules for electric dipole transitions among D_{3h} irreducible representations. Thus, these selection rules provide some help in the identification of specific transitions. It seems clear that the $^3P_0$ state, which transforms as the Γ_1 representation, lies above the ground state by about 20,785 cm^{-1} at low temperature, and the polarization of the absorption lines terminating on it indicates that the ground state and 190 cm^{-1} excited state both have representation Γ_6. The weak σ-polarized absorption peaks evident in figure 3 at 479.1 and 476.6 nm could represent transitions to $^1I_6$ states, transitions to the $^3P_0$ level in perturbed sites, or vibronic transitions associated with the 481.1-nm $^3P_0$ line. These peaks are stronger relative to the 481.1-nm absorption line in 5-percent Pr,Mg:SAM than in 1-percent samples, which is consistent with either of the latter two possibilities [20]. (The dependence of vibronic transition strength on concentration is attributed [20] to exchange effects between nearby Pr ions.) The existence of very similarly spaced peaks above the energy of the higher energy (440.9 nm) of the two σ-polarized $^3P_2$ lines favors the vibronic interpretation. Strong transitions near 466 nm mark the position of the $^3P_1$ manifold, and weaker transitions

6

between 454 and 469 nm are probably due to $^1I_6$ states, although vibronic and perturbed site electronic transitions to $^3P_1$ may also be present. In addition to the 486-nm σ-polarized hot-band absorption line, several other hot bands in both polarizations are consistent with the 190-cm^{-1} Γ_6 initial state. Other hot bands indicate the presence of at least one level about 200 to 250 cm^{-1} above the ground state, probably a Γ_3, whereas for still other hot bands, the levels are more difficult to identify.

4. Emission Spectroscopy

Figure 4 presents the room-temperature σ and π emission spectra of 1-percent Pr,Mg:SAM upon Xe lamp excitation at 455 nm. These spectra have been corrected for the wavelength and polarization response of the detection system, and are thus proportional to power emitted per unit interval of wavelength. The position and polarization of the strongest peak makes it clear that it is the reverse of the room-temperature "hot band" absorption at 486 nm. This line dominates the emission from $^3P_0$ (and $^3P_1$, $^3P_2$, and $^1I_6$) to the $^3H_4$ manifold, which is in turn stronger than emission to the $^3H_5$, $^3H_6$, and $^3F_2$ manifolds. The fluorescence at wavelengths longer than 665 nm (detected by photomultiplier tube, Ge detector, or both) is so much weaker as to be negligible.

Figure 5 shows the unpolarized room-temperature emission from 1-percent Pr,Mg:SAM upon excitation into the $^1D_2$ manifold. This weak emission is attributable to the $^1D_2 \rightarrow {}^3H_4$ transition. Transitions from $^1D_2$ to other manifolds are too weak for reliable detection. Comparison of figures 4 and 5 indicates that emission from $^1D_2$ makes a negligible contribution to the spectra of figure 4.

The $^3P_0$ fluorescence from samples with 5- or 10-percent Pr is quite similar to these data, except that the fluorescence line near 486 nm is much less strong relative to the other lines than in the 1-percent sample. In view of the room-temperature absorption at that wavelength, this reduced strength is attributable to reabsorption. Estimates of the percentage absorbed at that peak wavelength for light emitted from the center of the 5.9-mm-thick 1-percent Pr,Mg:SAM sample indicate that reabsorption should not be significant in that sample. To further reduce the problem, we took the data of figure 4 by exciting the surface facing the detection system, in such a geometry that only the front millimeter or less was excited.

Figure 4. Room-temperature $^3P_0$ fluorescence of a 1-percent Pr,Mg:SAM sample, corrected for instrument response. Baselines are offset for clarity.
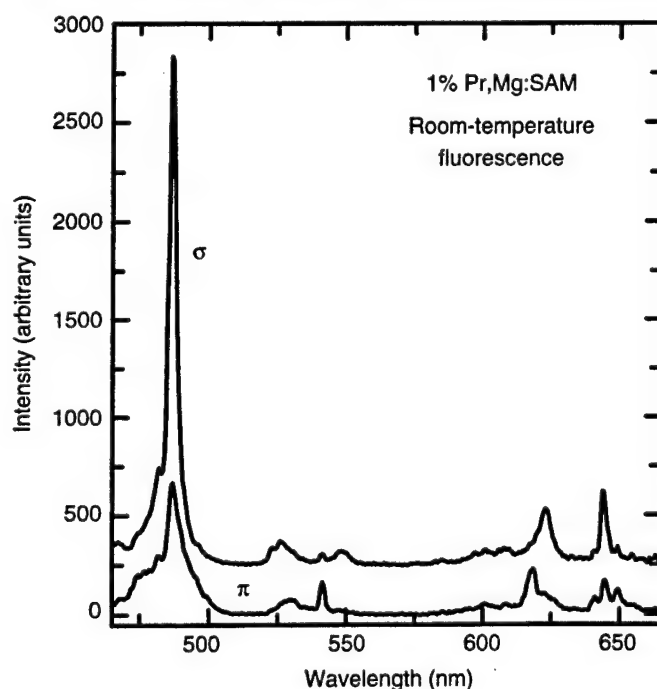
The fluorescence branching ratios from the $^3P_0$ (and thermally populated higher levels) to the lower manifolds may be estimated from these data. The signal for the fluorescence terminating on each manifold was integrated over wavelength, averaged over polarizations by the addition of two-thirds of the σ signal to one-third of the π signal, then multiplied by the average wavelength of the band to give a result proportional to transition rate rather than emitted power. Division by the sum over all emission bands yielded the experimental branching ratios reported in table 2. The predominance of emission to the $^3H_4$ manifold is clear, but the emission to $^3H_6$ is also substantial.

Figure 5. Unpolarized room-temperature fluorescence of 1-percent Pr,Mg:SAM upon pulsed excitation at 595 nm. Signal detected 30 μs after laser pulse, corrected for instrument response.
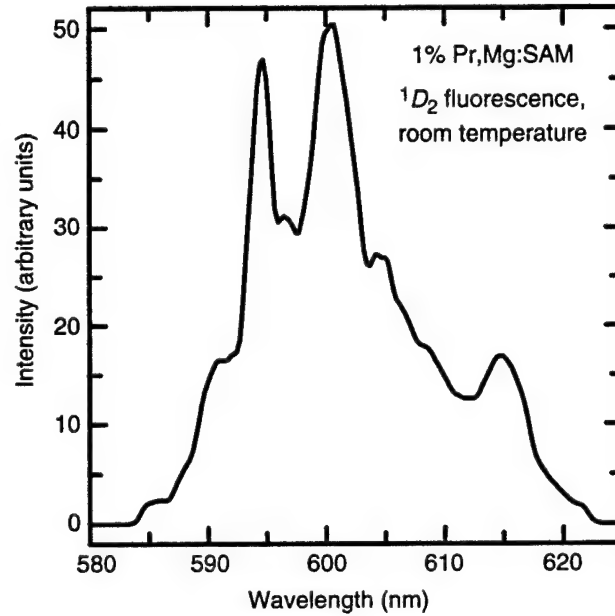
Table 2. Branching ratios and predicted radiative lifetimes for room-temperature fluorescence from Pr,Mg:SAM $^3P_0$ and nearby manifolds to lower manifolds. Predictions are based on modified Judd-Ofelt model and parameters from final column, table 3.

| | | | Predicted branching ratio | |
Final manifold	Approximate wavelength (nm)	Experimental branching ratio	if only $^3P_0$ is populated	with 70% $^3P_0$, 20% $^1I_6$, 10% $^3P_1$ population
$^3H_4$	487	0.60	0.47	0.40
$^3H_5$	540	0.09	0.00	0.05
$^3H_6$	620	0.20	0.29	0.26
$^3F_2$	645	0.11	0.13	0.11
$^3F_3 + {}^3F_4$	710	~0	0.10	0.14
$^1G_4$	930	~0	0.01	0.04
$^1D_2$	2600	assumed 0	0.00	0.00
			$\tau_{rad} = 36$ μs	$\tau_{rad} = 42$ μs

9

5. Decay Kinetics

Figure 6 shows the room-temperature fluorescence decay waveforms of the $^3P_0$ and $^1D_2$ manifolds for 1- and 5-percent Pr samples. The $^3P_0$ decay waveforms do not deviate greatly from single exponential at any temperature, even at 10-percent concentration. That is, the "effective lifetime"—defined as the time-integrated fluorescence signal divided by the initial signal—is shorter than the exponential that dominates at long times by only 10 to 30 percent. Further, the $^3P_0$ effective lifetime decreases only modestly with increasing concentration.

The $^1D_2$ decay behaves quite differently. The nearly single exponential decay observed in 1-percent Pr,Mg:SAM becomes highly nonexponential with a much shorter effective lifetime in 5-percent Pr,Mg:SAM. No $^1D_2$ fluorescence has been detected in the 10-percent Pr samples, indicating even more severe quenching. The decay behavior of both $^3P_0$ and $^1D_2$ manifolds is summarized in figure 7.

The sharp difference in concentration dependence of decay from these two manifolds indicates that the $^3P_0$ state is far more resistant to concentration quenching than the $^1D_2$. One possible reason for this would be strongly differing degrees of energy mismatch for cross relaxation between Pr ions. However, the observed absorption lines of Pr^{3+} in SAM indicate that nearly perfect resonance (energy mismatches of only several wavenumbers) exists for both the $(^3P_0, {}^3H_4) \rightarrow (^1G_4, {}^1G_4)$ and the $(^1D_2, {}^3H_4) \rightarrow (^1G_4, {}^3F_4)$ cross-relaxation processes. We initially suspected spin selection rules of causing the strong difference in susceptibility to concentration quenching [14]. This explanation suggested itself because in the above processes, which are much more nearly resonant than any other cross-relaxation channels from these initial states, the $^1D_2$ decay can occur in such a way as to involve spin-allowed transitions on both ions, whereas the $^3P_0$ decay process

Figure 6. Room-temperature fluorescence decay curves for two different excited states of Pr,Mg:SAM, $^3P_0$ (plus thermally populated $^3P_1$ and $^1I_6$ states) and $^1D_2$, and two different Pr^{3+} concentrations.
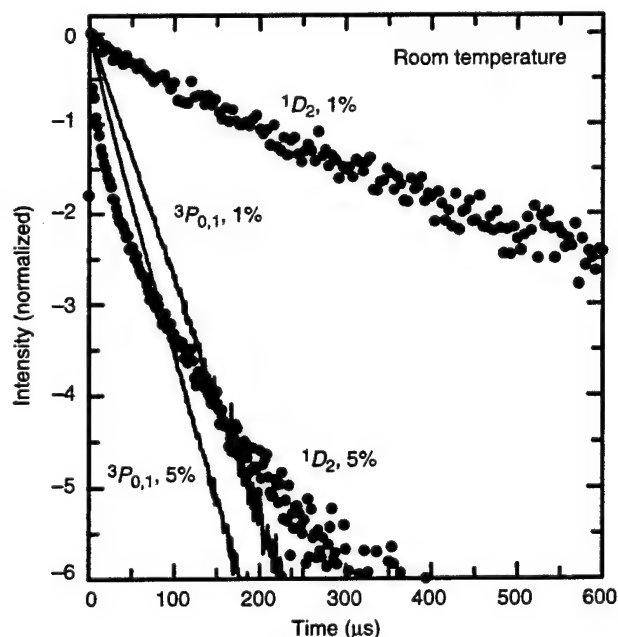
requires a spin-forbidden transition (to first approximation) on each ion. However, the total spin for the two-ion system can be conserved in the $(^3P_0, {}^3H_4) \rightarrow (^1G_4, {}^1G_4)$ process, so this explanation must also be rejected. A much more detailed understanding of the linestrengths for the specific transitions involved in each cross-relaxation process may be required for us to understand the differences in concentration-dependent quenching. Such detailed investigation is beyond the scope of the present study.

Figure 7 also shows that the temperature dependence for decay of both $^3P_0$ and $^1D_2$ is relatively weak, suggesting that intraionic radiationless relaxation from either manifold is not strong, at least up to room temperature. This perhaps is not surprising in view of the large energy gaps separating both $^3P_0$ and $^1D_2$ from the next lower manifolds. It should be remembered, however, that for the samples with higher Pr concentration, reabsorption of the strongest $^3P_0$ emission line becomes substantial at room temperature. Since this reabsorption can lengthen the observed lifetime, it is possible that the $^3P_0$ emission quenches somewhat more strongly with temperature at high concentrations than the data indicate [21]. Given the lack of such reabsorption at low temperature and its weakness in the 1-percent sample, it seems reasonable to take the single-exponential tail decay time for the 1-percent sample as an estimate of the radiative lifetime of the $^3P_0$ state in Pr,Mg:SAM. This value is about 38 μs for all temperatures up to room temperature.

We have also measured the room-temperature fluorescence decay waveforms of the $^3P_0$ state (plus any thermally populated $^3P_1$ and $^1I_6$ states) for Pr,Mg:BaAl$_{12}$O$_{19}$ (Pr,Mg:BAM) and Pr,Mg:CaAl$_{12}$O$_{19}$ (Pr,Mg:CAM). Despite the 8-at.% Pr and Mg concentrations in the starting materials, so little Pr^{3+} entered these samples that absorption spectra exhibit no Pr^{3+} features, and only crude, low-resolution fluorescence spectra have been obtained. However, with pulsed dye laser excitation near 470 nm and wide mono-

Figure 7. Pr,Mg:SAM effective lifetime versus temperature.
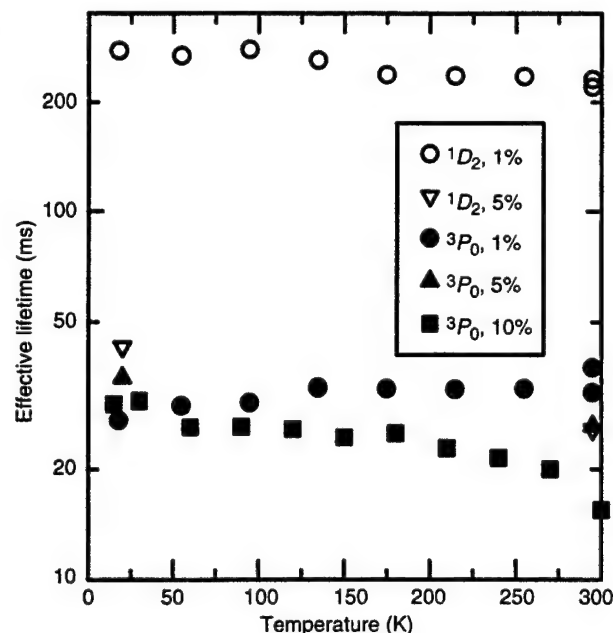
chromator slits, we could obtain lifetime data. The decay waveform of Pr,Mg:BAM is approximately single exponential with a lifetime of about 19 μs. That of Pr,Mg:CAM is discernibly nonexponential, with a tail decay time of about 23 μs and an effective lifetime of about 20 μs. These lifetimes are shorter and thus less attractive than that of low-concentration Pr,Mg:SAM. As a result, we have done no further study of Pr,Mg:CAM and Pr,Mg:BAM.

6. Judd-Ofelt Analysis

The theory of Judd and Ofelt, which has been applied and conveniently summarized by Lomheim and DeShazer [22], provides a useful way to characterize the room-temperature absorption data and to predict excited-state radiative lifetimes. The data must first be averaged over polarizations, which we have done simply by integrating the absorption coefficient over a given absorption band for each polarization, then taking two-thirds of the value for σ-polarization plus one-third of the value for π-polarization. This is more accurate than the more complicated expression used by Lomheim and DeShazer, which depends on a macroscopic property (sample thickness) [22].

Difficulty is often encountered in applying Judd-Ofelt theory to Pr^{3+}, namely, the appearance of an unphysical negative value for the parameter Ω_2. Indeed, in Pr,Mg:SAM we obtain $\Omega_2 = -6 \times 10^{-22}$ cm^2, $\Omega_4 = 1.68 \times 10^{-20}$ cm^2, and $\Omega_6 = 3.62 \times 10^{-20}$ cm^2. This difficulty is often caused by stronger $^3H_4 \rightarrow {}^3P_2$ absorption than can be accommodated by the Judd-Ofelt theory, yet in our case deletion of the $^3P_2$ absorption from the data set changes the Ω's only negligibly.

Recently two very different approaches have been used to address this difficulty [23,24]. Dunina et al [23] attribute the Ω_2 problem in part to the relatively low energy of the lowest $4f5d$ state, whose mixing with the $4f^2$ states in noncentrosymmetric sites breaks down the parity selection rule for $f \rightarrow f$ transitions. Its low energy tends to make absorption transitions to high-lying $4f^2$ states, including $^3P_2$, stronger relative to transitions to low-lying states than predicted by Judd-Ofelt theory, which neglects the energy of the opposite-parity states. We express the modification made by Dunina et al to account for the finite $4f5d$ energy as follows:

$$S(i,j) = \Sigma_{\lambda=2,4,6} \Omega'_\lambda \langle i | U^\lambda | j \rangle^2 \left[1 + \left(E_i + E_j - 2E_f^0 \right) \left(E_{5d} - E_f^0 \right) \right] . \tag{2}$$

Here $S(i,j)$ is the linestrength for the transition from manifold i to manifold j, $\langle i | U^\lambda | j \rangle^2$ is the same squared, reduced-matrix element used in the standard Judd-Ofelt theory [25], E_i, E_j, and E_{5d} are the energies of the initial state, final state, and lowest $4f5d$ state, respectively, and E_f^0 is the average energy over all the optically accessible $4f^2$ states. Ω'_λ for $\lambda = 2$, 4, and 6 are the Judd-Ofelt fitting parameters for this modified theory. Using this modified theory, we obtained a positive value for each Ω'_λ. The results are presented in table 3.

Quimby and Miniscalco [24] report that the inclusion of fluorescence branching ratio data in the Judd-Ofelt fitting procedure improves the quality of the fit by increasing the number of data points to be fit and decreasing the relative importance of ill-behaved transitions such as $^3H_4 \rightarrow {}^3P_2$. We have used the textbook relationship between linestrength and transition rate to relate the observed fluorescence branching ratios to the linestrengths predicted by the Judd-Ofelt theory and published reduced matrix elements for emission [22,25,26]. The matrix elements for emission

13

Table 3. Absorption transition strength data and results of fits to modified Judd-Ofelt theory. For modification of Dunina et al [23], E_{5d} is taken to be 47,000 cm^{-1} and E_f^0 to be 11,570 cm^{-1}. Method of Quimby and Miniscalco [24] fits $^3P_0$ fluorescence branching ratios as well as absorption linestrengths.

| Final manifold | Average wave-length (nm) | Linestrength (10^{-20} cm^2) | | | |
		Observed, $S(i,f)_e$	Dunina fit, $S(i,f)_{t,d}$ and Ω's	Quimby fit, $S(i,f)_{t,q}$ and Ω's	Fit using both mod's, $S(i,f)_{t,dq}$ and Ω's
Ω_2'	—	—	1.38	0.15	0.84
Ω_4'	—	—	1.53	1.52	2.19
Ω_6'	—	—	7.03	3.64	6.86
RMS error	—	—	0.10	0.09	0.10
Absorption to—					
$^3H_6$	2450	0.425	0.496	0.559	0.495
$^3F_2$	1910	1.073	1.072	1.118	1.059
$^3F_3 + {}^3F_4$	1500	4.937	4.870	4.932	4.901
$^1G_4$	1000	0.128	0.127	0.108	0.127
$^1D_2$	600	0.217	0.328	0.215	0.328
$^3P_0$	485	0.223	0.248	0.262	0.350
$^3P_1 + {}^1I_6$	471	0.513	0.519	0.426	0.618
$^3P_2$	444	0.716	0.992	0.549	0.991
Emission from $^3P_0$ to—					
$^3H_4$	487	—	—	0.26 (0.28)[a]	0.37 (0.50)
$^3H_6$	620	—	—	0.26 (0.19)	0.49 (0.34)
$^3F_2$	645	—	—	0.04 (0.12)	0.26 (0.21)

[a]Parenthetical values were obtained by conversion to relative linestrengths and multiplication by best-fit $^3P_0 \rightarrow {}^3F_2$ linestrength. Other emission entries are Judd-Ofelt predictions from best-fit Ω_λ' parameters.

from the ^3P_J and $^1I_6$ manifolds indicate that if $^1I_6$ levels lay as low as the observed 476.6- and 479.1-nm absorption lines, then emission to the $^1G_4$ and $^3F_3 + {}^3F_4$ manifolds would be as strong as that to the $^3H_4$ and $^3H_6$ manifolds, contrary to the observed pattern. We therefore assume that those absorption lines are due to $^3P_0$ transitions, whether vibronic or minority site electronic, and that the $^1I_6$ levels do not extend below the energy of the absorption lines near 469 nm. This means that at room temperature, most excited Pr^{3+} ions are in the $^3P_0$ state, and for simplicity, only that excited state was considered in the Judd-Ofelt fitting of fluorescence data. Only the three strongest emission bands (those terminating on $^3H_4$, $^3H_6$, and $^3F_2$) were used in the fitting, and to relate observed branching ratios to calculated linestrengths, we treated the linestrength of the $^3P_0 \rightarrow {}^3F_2$ band as a fitting parameter. We then adjusted this parameter and the three Ω_λ' values to minimize the sum of the squared differences between observed and predicted absorption and emission linestrengths.

Table 3 presents the results of fitting the experimental data using only the Quimby-Miniscalco approach, and also the results using both this and the Dunina et al modification. The emission entries not in parentheses are the Judd-Ofelt predictions using the best-fit Ω_λ' parameters. The entries in

parentheses are those obtained from the observed branching ratios by conversion to relative linestrengths and multiplication by the best-fit $^3P_0 \rightarrow {}^3F_2$ linestrength. In the quoted root mean square deviations between theory and experiment, we include the absorption transitions only, to facilitate comparisons among the different fits. This deviation is about the same for all three approaches.

These three approaches to Judd-Ofelt fitting give different predictions for the radiative lifetime of the $^3P_0$ state. The fit using only the Dunina et al modification predicts a lifetime of 39 µs, that using only Quimby and Miniscalco's approach predicts 61 µs, and that incorporating both modifications predicts 36 µs. If we compare with the data of section 5, it appears that the Dunina et al correction for finite $4f5d$ energy is necessary to achieve a reasonable prediction of the radiative lifetime. The fit including both the Dunina et al and Quimby and Miniscalco modifications appears to give the best overall fit to absorption, branching ratio, and lifetime data.

Table 2 (sect. 4) shows the predicted fluorescence branching ratios and radiative lifetime obtained with that fit. Two cases are considered: one with all excited ions in the $^3P_0$, and the other with room-temperature thermal population of the $^1I_6$ manifold (its states assumed to be equally spaced between 21,330 and 22,000 cm^{-1}) and of the $^3P_1$ (taken to lie at 21,420 cm^{-1}). The agreement between observed and predicted branching ratios is fair at best, indicating that the Judd-Ofelt model, even as modified, still describes Pr^{3+} only poorly. We may somewhat alleviate the too-large predictions for branching ratios to the $^1G_4$ and $^3F_3 + {}^3F_4$ manifolds when $^3P_1$ and $^1I_6$ are included, and the underestimate of fluorescence to $^3H_5$, if we place the bottom of the $^1I_6$ manifold above the $^3P_1$. The large discrepancy in the branching ratio to $^3H_4$ may result from the fact that the strongest transition between $^3P_0$ and $^3H_4$ involves a $^3H_4$ state 190 cm^{-1} above the ground state. As a result, its thermal population at room temperature is modest, reducing the effective cross section for absorption from this state but not that for emission to it. Thus, fitting the room-temperature $^3P_0$ absorption tends to favor a smaller value of Ω_4'/Ω_2' than would be required to fit the large $^3P_0 \rightarrow {}^3H_4$ branching ratio.

7. Laser Parameters and Experiments

With the fluorescence data of section 4 and the estimate of the radiative lifetime from section 5, it is possible to estimate the effective stimulated emission cross sections of the main emission peaks. The standard relationships between radiative decay rate and stimulated emission cross section give the following:

$$1/\tau_{rad} = \Sigma_i \Sigma_j W_{rad, ij} = \Sigma_i \Sigma_j 8\pi\sigma_{se}(v_{pk})_{ij} \Delta v_{eff}/3(\lambda_{i, vac}/n_{ij})^2 . \qquad (3)$$

Here $1/\tau_{rad}$ is the total radiative decay rate, and the sums over i and j extend over all final manifolds to which fluorescence occurs and the three possible electric-field polarizations (two σ's and one π), respectively. For emission band i and polarization j, $W_{rad,ij}$ is the radiative decay rate, $\sigma_{se}(v_{pk})_{ij}$ is the stimulated emission cross section at the frequency of peak intensity, $\lambda_{i,vac}$ is the vacuum wavelength corresponding to that frequency, and n_{ij} is the index of refraction at that wavelength. Δv_{eff} is the effective width of the ij^{th} emission band, defined as the fluorescence intensity integrated over that band, divided by the peak intensity.

As in the Judd-Ofelt calculations, we here approximate the index versus wavelength λ for both polarizations by $n(\lambda) = 1.75 + (12{,}700 \text{ nm}^2)/\lambda^2$; we obtain this value by fitting the published n versus λ data on the closely related crystal $LaMgAl_{11}O_{19}$ [27]. The experimental branching ratios from table 2 and the estimated radiative lifetime from section 5 permit the elimination of the sum over final manifolds. The relative intensities for the different polarizations can then be used to obtain the W_{ij} values for the strongest emission transitions. These, the effective linewidths, and the resulting effective stimulated emission cross sections are given in table 4.

Extraction of the actual cross sections from the observed "effective" cross sections requires correction for thermal population of the initial state, which can at present only be estimated because of our incomplete knowledge of the energy levels. For the $^3P_0$ state, we use the two different cases of table 2 for this estimate. Thus, for example, the actual stimulated emission cross section for the 486-nm σ-polarized peak is estimated to be 1.0 to

Table 4. Room-temperature effective stimulated emission cross sections of Pr,Mg:SAM, estimated from fluorescence data. Decay rates refer to total emission in given polarization to given final manifold. In each case, initial state is $^3P_0$ (plus thermally populated $^3P_1$ and $^1I_6$ states).

Final manifold	Peak wavelength (nm)	Polarization	Decay rate (s⁻¹)	Effective linewidth (10^{12} Hz)	Peak $\sigma_{se,eff}$ (10^{-20}cm²)
$^3H_4$	486.0	σ	6180	7.2	10.5
$^3H_5$	541.5	π	670	9.2	1.1
$^3H_6$	618.5	π	1470	9.5	3.0
$^3H_6$	623.5	σ	1990	10.2	3.9
$^3F_2$	644.0	σ	1020	3.6	6.1

1.5×10^{-19} cm^2. Note that if the observed low-concentration fluorescence lifetime is shortened by nonradiative processes (thus giving a fluorescence quantum efficiency substantially less than one), the above cross-section estimates will be too large.

This result can be checked if one estimates the stimulated emission cross section at the 486-nm peak from the absorption data. Polarization data indicate that the lower level of this transition is the doubly degenerate Γ_6. The thermal population of this 190-cm^{-1} Γ_6 state has been estimated for two simple models, constrained by the observation of at least one additional $^3H_4$ state near 200 to 250 cm^{-1}. Each model assumes that about half the $^3H_4$ states other than the Γ_6 states lie near the 190-cm^{-1} state, but one model places the other half near the ground state, so that their thermal population at room temperature is high, and the other places them too high to be significantly populated at room temperature. The resulting estimates of the fraction of Pr ions thermally populating the 190-cm^{-1} state are 0.15 and 0.20. With these estimates, the observed effective ground-state absorption cross section of the 486.5-nm peak at room temperature, 1.2×10^{-20} cm^2, indicates a true absorption cross section of 6.0 to 8.0×10^{-20} cm^2. In view of the degeneracies of the states, this yields a stimulated emission cross section of 1.2 to 1.6×10^{-19} cm^2 predicted from the absorption data. The agreement with the estimates based on fluorescence is quite satisfactory, and supports the assumption that the $^3P_0$ fluorescence quantum efficiency in the 1-percent Pr sample is high.

Simple laser-pumped laser experiments have been performed on samples of 5-percent Pr,Mg:SAM. Early experiments were performed on samples with poorly polished, uncoated surfaces. These samples did not exhibit laser action at room temperature, but did so at cryogenic temperatures where narrowing of the emission lines provided higher stimulated emission cross sections. A 0.46-cm-thick sample was placed in an optical cryostat with uncoated fused silica windows inside a laser cavity about 23 cm long. One cavity mirror was flat, coated for high reflectivity between 600 and 640 nm, with about 90-percent transmission between 450 and 510 nm to permit end pumping. The other mirror had a 25-cm radius of curvature and was coated to give about 99-percent reflectivity at 620 nm. The sample was pumped through the flat mirror by 466-nm, σ-polarized pulses obtained by high-pressure H$_2$ anti-Stokes Raman shifting of the output of the Continuum Nd:YAG-pumped dye laser system. The pump light was focused into the sample by a lens of 8-cm focal length. Laser output was observed for temperatures up to 120 K at about 641 nm, which table 4 shows to have the highest stimulated emission cross section in the spectral region of the mirrors. The laser performance at 15 K is shown in figure 8.

Blue-green laser oscillation at 15 K was also occasionally observed. This output did not depend on the presence of the cavity mirrors, indicating that the gain was high enough to support oscillation with the feedback from the uncoated sample surfaces. Since a crude wavelength measurement showed the output wavelength to be near 480 nm, this must surely be due to the strong emission peak at about 486 nm.

17

We also carried out laser experiments at room temperature on samples of 5-percent Pr,Mg:SAM with surfaces better polished and antireflection coated for 620 nm. So that larger pump energies could be obtained, the sample was end-pumped by a dye laser operating with Coumarin dye and pumped by a frequency-tripled Nd:YAG laser. The dye tuning range required pumping the 486-nm absorption peak. As in the low-temperature experiments, considerable care was needed to find regions of the sample that would support laser action, because of inhomogeneities in the crystals. For this reason, better room-temperature performance was obtained with a sample only 0.2 cm thick than with a thicker sample, despite the smaller fraction of pump light absorbed. In fact, when room-temperature laser action was obtained in a thicker sample, the very bad (many-lobed) beam quality made it clear that sample inhomogeneities were substantial. Figure 8 shows the room-temperature laser performance for the 0.2-cm-thick sample.

We made attempts at room-temperature blue-green laser action using cavity mirrors coated for high reflection and 99-percent reflection at 480 nm. The pump beam was directed onto the sample at a sufficient angle to miss the cavity mirrors. No laser output was observed, probably because of the large room-temperature absorption at 486 nm. Estimates based on the effective absorption and stimulated emission cross sections indicate that a population inversion of about 12 percent would be needed to reach threshold on this transition, and that this would require several millijoules of pump energy under our experimental conditions.

Figure 8. 5-percent Pr,Mg:SAM laser performance for red output (approximately 641 nm). For 15 K data, sample was uncoated and pump wavelength was 466 nm. For room-temperature data, sample was antireflection coated and pumped at 486 nm.
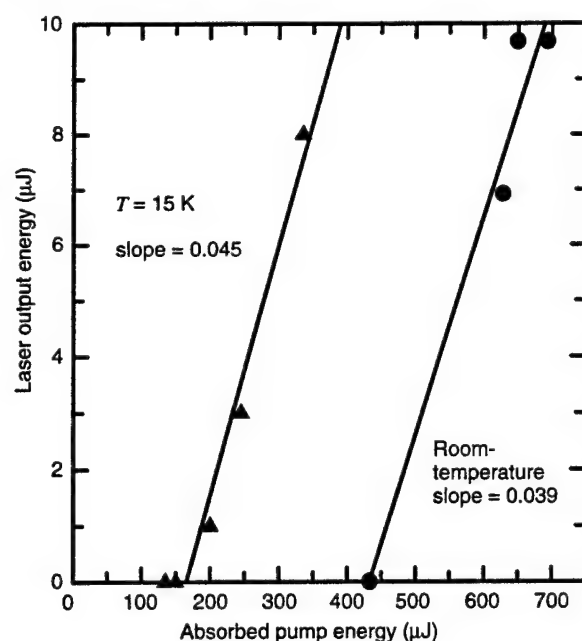
8. Conclusions

The spectroscopic properties of Pr,Mg:SAM relevant to laser action are, on the whole, quite favorable. As anticipated based on the large Sr-O distances in this host, the Pr^{3+} $^3P_0$ radiative lifetime is rather long for an oxide, almost as long as that of Pr:YLiF$_4$ [6]. Of course, for Q-switched laser operation it would be desirable to have a still longer lifetime, requiring a still weaker crystal field or a site with higher symmetry. However, Pr,Mg:SAM represents a very promising step in this direction as compared to Pr:YAG or Pr:YAlO$_3$. Despite the long lifetime, the estimated stimulated emission cross sections of the stronger $^3P_0$ emission lines are reasonable. The minimal concentration and thermal quenching of the $^3P_0$ even at several percent replacement of Sr by Pr makes it possible to dope the crystal heavily enough for good pump absorption.

Laser operation in the red has been demonstrated at room temperature and in the blue-green at low temperature, indicating that excited-state absorption from the $^3P_0$ state must not be prohibitive at these wavelengths. This is consistent with our expectation based on the relatively high onset energy for ground-state absorption to the $4f5d$ states. The laser efficiency observed thus far is very low, however, and excited-state absorption cannot be ruled out as a cause. In view of the observed inhomogeneities in the samples, though, this inefficiency may be due in large part to bulk scattering losses. Thus, further refinement of the crystal growth parameters may permit substantially improved laser performance.

References

1. L. Esterowitz, R. Allen, M. Kruer, F. Bartoli, L. S. Goldberg, H. P. Jenssen, A. Linz, and V. O. Nicolai, "Blue Light Emission by a Pr:LiYF$_4$ Laser Operated at Room Temperature," J. Appl. Phys. **48**, 650 (1977).

2. A. A. Kaminskii, A. G. Petrosyan, K. L. Ovanesyan, and M. I. Chertanov, "Stimulated Emission of Pr^{3+} Ions in YAlO$_3$ Crystals," Phys. Status Solidi (a) **77**, K173 (1983).

3. D. S. Knowles, Z. Zhang, D. Gabbe, and H. P. Jenssen, "Laser Action of Pr^{3+} in LiYF$_4$ and Spectroscopy of Eu^{2+}-Sensitized Pr in BaY$_2$F$_8$," IEEE J. Quantum Electron. **24**, 1118 (1988).

4. A. A. Kaminskii, "New Room-Temperature Stimulated-Emission Channels of Pr^{3+} Ions in Anisotropic Laser Crystals," Phys. Status Solidi (a) **125**, K109 (1991).

5. T. Sandrock, T. Danger, E. Heumann, G. Huber, and B.H.T. Chai, "Continuous Wave Laser Action of Pr-Doped Fluorides at Room Temperature," in *OSA Proceedings on Advanced Solid-State Lasers*, T. Y. Fan and B.H.T. Chai, eds. (Optical Society of America, Washington, DC, 1994), **20**, p 357.

6. M. Malinowski, M. F. Joubert, R. Mahiou, and B. Jacquier, "Visible Laser Emission of Pr^{3+} in Various Hosts," J. Phys. Paris IV **C4**, C4-541 (1994).

7. A. J. Lindop, C. Matthews, and D. W. Goodwin, "The Refined Structure of SrO·6Al$_2$O$_3$," Acta Crystallogr. **B31**, 2940 (1975).

8. S. Alablanche, R. Collongues, M. Leduc, A. Minvielle, J. Théry, and D. Vivien, "Tunable Laser Effect in ASN a Neodymium-Activated Strontium-Magnesium Hexaaluminate," J. Phys. Paris IV **C7**, C7-275 (1991).

9. A. Kahn, A. M. Lejus, M. Madsac, J. Théry, D. Vivien, and J. C. Bernier, "Preparation, Structure, Optical, and Magnetic Properties of Lanthanide Aluminate Single Crystals (LnMAl$_{11}$O$_{19}$)," J. Appl. Phys. **52**, 6864 (1981).

10. R.W.G. Wyckoff, *Crystal Structures* (Wiley, New York, 1965), **3**, p 222.

11. V. Delacarte, J. Théry, and D. Vivien, "Optical Fluorescence and Fluorescence Dynamics of Nd^{3+} in Sr$_{1-x}$Nd$_y$La$_{x-y}$Mg$_x$Al$_{12-x}$O$_{19}$ (ASL:Nd)," J. Lumin. **62**, 237 (1994).

12. R. Collongues and D. Vivien, "Lanthanum Magnesium Aluminate (LMA) and Its Derivatives: An Example of Laser Materials Engineering," J. Solid State Chem. **96**, 97 (1992).

13. L. D. Merkle, B. Zandi, Y. Guyot, H. R. Verdun, B. McIntosh, B.H.T. Chai, J. B. Gruber, M. D. Seltzer, C. A. Morrison, and R. Moncorgé, "Spectroscopic Study of Pr:Ca$_5$(PO$_4$)$_3$F and Pr:SrAl$_{12}$O$_{19}$ as Potential Visible Laser Materials," in *OSA Proceedings on Advanced Solid-State Lasers*, T. Y. Fan and B.H.T. Chai, eds. (Optical Society of America, Washington, DC 1994), **20**, p 361.

14. Larry D. Merkle, Bahram Zandi, Richard Moncorgé, Yannick Guyot, Horacio R. Verdun, and Bruce McIntosh, "Spectroscopy and Laser Operation of Pr,Mg:SrAl$_{12}$O$_{19}$," J. Appl. Phys. **79**, 1849 (1996).

15. K. Spariosu, R. D. Stultz, M. Birnbaum, T. H. Allik, and J. A. Hutchinson, "Erbium Doped Calcium Phosphate Fluoride (Er:Ca$_5$(PO$_4$)$_3$F) Saturable-Absorber Q-Switch for the Erbium Glass Laser at 1.53 μm," Appl. Phys. Lett. **62**, 2763 (1993).

16. J. Ganem, W. M. Dennis, and W. M. Yen, "One-Color Sequential Pumping of the 4f5d Bands in Pr-Doped Yttrium Aluminum Garnet," J. Lumin. **54**, 79 (1992).

17. Y. M. Cheung and S. K. Gayen, "Excited-State Absorption in Pr^{3+}: Y$_3$Al$_5$O$_{12}$," Phys. Rev. B **49**, 14,827 (1994).

18. C. A. Morrison, "Host Dependence of the Rare-Earth Ion Energy Separation 4f^N–4$f^{N-1}nl$," J. Chem. Phys. **72**, 1001 (1980).

19. J. Sugar and J. Reader, "Ionization Energies of Doubly and Triply Ionized Rare Earths," J. Chem. Phys. **59**, 2083 (1973).

20. A. Meijerink, C. de Mello Donegá, A. Ellens, J. Sytsma, and G. Blasse, "Vibronic Transitions of Rare Earth Ions," J. Lumin. **58**, 26 (1994).

21. D. S. Sumida and T. Y. Fan, "Impact of Radiation Trapping on Fluorescence Lifetime and Stimulated Emission Cross Section Measurements in Solid-State Laser Media," Opt. Lett. **19**, 1343 (1994).

22. T. S. Lomheim and L. G. DeShazer, "Optical-Absorption Intensities of Trivalent Neodymium in the Uniaxial Crystal Yttrium Orthovanadate," J. Appl. Phys. **49**, 5517 (1978).

23. E. B. Dunina, A. A. Kaminskii, A. A. Kornienko, K. Kurbanov, and K. K. Pukhov, "The Dependence of the Line Strength of Electric Dipole f–f Transitions on the Manifold Energy of the Pr^{3+} Ion in YAlO$_3$," Sov. Phys. Solid State **32**, 920 (1990) [transl. of Fiz. Tverd. Tela (Leningrad) **32**, 1568 (1990)].

24. R. S. Quimby and W. J. Miniscalco, "Modified Judd-Ofelt Technique and Application to Optical Transitions in Pr^{3+}-Doped Glass," J. Appl. Phys. **75**, 613 (1994).

25. A. A. Kaminskii, *Laser Crystals*, second ed. (Springer-Verlag, Berlin, 1990), pp 154–158.

26. M. J. Weber, "Spontaneous Emission Probabilities and Quantum Efficiencies for Excited States of Pr^{3+} in LaF$_3$," J. Chem. Phys. **48**, 4774 (1968).

27. P. I. Bykovskii, V. A. Lebedev, V. F. Pisarenko, and V. V. Popov, "Structures and Luminescence Spectra of Hexagonal Rare-Earth Aluminates (Review)," J. Appl. Spectrosc. **44**, 425 (1986) [transl. of Zh. Prikl. Specktrosk. **44**, 711 (1986)].

Distribution

Admnstr
Defns Techl Info Ctr
Attn DTIC-OCP
8725 John J Kingman Rd Ste 0944
FT Belvoir VA 22060-6218

Hdqtrs Dept of the Army
Attn DAMO-FDQ MAJ M McGonagle
Attn DAMO-FDQ D Schmidt
400 Army Pentagon
Washington DC 20310-0460

Nav Air Warfare Ctr
Attn 47423OD M Seltzer
1 Administration Circle
China Lake CA 93555-6001

Laboratoire de Physico-Chimie des Matériaux
  Luminescents
Université de Lyon I, URA 442 du CNRS
Attn R Moncorgé
Attn Y Guyot
43 bd du 11 Novembre 1918
Villeurbanne 69622
France

San Jose State Univ
Dept of Physics
Attn J B Gruber
One Washington Square
San Jose CA 95192-0106

Univ of Southern California
Attn M Birnbaum
Center for Laser Studies Univ Park
Los Angeles CA 90089

Fibertek Inc
Attn H Verdun
510 Herndon Parkway
Herndon VA 22070

US Army Rsrch Lab
Attn AMSRL-SE-EO G Wood
Attn AMSRL-SE-EO L Merkle (5 copies)
Attn AMSRL-SE-EO B Zandi (5 copies)
Bldg 357
FT Belvoir VA 22060

US Army Rsrch lab
Attn AMSRL-SE H Pollehn
10235 Burbeck Rd Ste 110
FT Belvoir VA 22060-5838

US Army Rsrch Lab
Attn J Zavada
PO Box 12211
Research Triangle Park NC 27709-2211

US Army Rsrch Lab
Attn AMSRL-CI-LL Tech Lib (3 copies)
Attn AMSRL-CS-AL-TA Mail & Records
  Mgmt
Attn AMSRL-CS-AL-TP Techl Pub
  (3 copies)
Attn AMSRL-SE-EP D Wortman
Attn AMSRL-SE-E J Pellegrino
Adelphi MD 20783-1197

REPORT DOCUMENTATION PAGE

Form Approved
OMB No. 0704-0188

Public reporting burden for this collection of information is estimated to average 1 hour per response, including the time for reviewing instructions, searching existing data sources, gathering and maintaining the data needed, and completing and reviewing the collection of information. Send comments regarding this burden estimate or any other aspect of this collection of information, including suggestions for reducing this burden, to Washington Headquarters Services, Directorate for Information Operations and Reports, 1215 Jefferson Davis Highway, Suite 1204, Arlington, VA 22202-4302, and to the Office of Management and Budget, Paperwork Reduction Project (0704-0188), Washington, DC 20503.

1. AGENCY USE ONLY (Leave blank)	2. REPORT DATE	3. REPORT TYPE AND DATES COVERED
	February 1997	Summary, June 1993–February 1996

4. TITLE AND SUBTITLE	5. FUNDING NUMBERS
Spectroscopic Studies and Laser Operation for Pr,Mg:SrAl$_{12}$O$_{19}$	DA PR: A31B PE: 61102A

6. AUTHOR(S)

Larry D. Merkle, Bahram Zandi (ARL), Richard Moncorgé, Yannick Guyot (Laboratoire de Physico-Chimie des Matériaux Luminescents), Horacio R. Verdun, and Bruce McIntosh (Fibertek, Inc.)

7. PERFORMING ORGANIZATION NAME(S) AND ADDRESS(ES)	8. PERFORMING ORGANIZATION REPORT NUMBER
U.S. Army Research Laboratory Attn: AMSRL-SE-EL 2800 Powder Mill Road Adelphi, MD 20783-1197	ARL-TR-1228

9. SPONSORING/MONITORING AGENCY NAME(S) AND ADDRESS(ES)	10. SPONSORING/MONITORING AGENCY REPORT NUMBER
U.S. Army Research Laboratory 2800 Powder Mill Road Adelphi, MD 20783-1197	

11. SUPPLEMENTARY NOTES

AMS code: 611102.31B11
ARL PR: A31B

12a. DISTRIBUTION/AVAILABILITY STATEMENT	12b. DISTRIBUTION CODE
Approved for public release; distribution unlimited.	

13. ABSTRACT (Maximum 200 words)

Pr^{3+}-doped $SrAl_{12}O_{19}$ has been investigated spectroscopically as a visible laser material. Its $^3P_0$ fluorescence lifetime is rather long for an oxide: about 35 µs. This excited state exhibits only mild concentration and temperature quenching, so that concentrations high enough to give good ground-state absorption into the ^3P_J manifolds still give strong, long-lived emission. Ground-state absorption into the $4f5d$ configuration begins at relatively high energy, so that excited-state absorption into this configuration is less likely to be significant at laser wavelengths in $SrAl_{12}O_{19}$ than in many other oxides, such as $Y_3Al_5O_{12}$. The stimulated emission cross sections of major emission lines have been estimated, and are quite reasonable for laser operation. Laser-pumped laser operation has been demonstrated in the red ($^3P_0 \rightarrow {}^3F_2$) at room temperature and in the blue-green ($^3P_0 \rightarrow {}^3H_4$) at cryogenic temperatures.

14. SUBJECT TERMS	15. NUMBER OF PAGES
Solid-state laser, laser materials, spectroscopy, praseodymium	29
	16. PRICE CODE

17. SECURITY CLASSIFICATION OF REPORT	18. SECURITY CLASSIFICATION OF THIS PAGE	19. SECURITY CLASSIFICATION OF ABSTRACT	20. LIMITATION OF ABSTRACT
Unclassified	Unclassified	Unclassified	UL

NSN 7540-01-280-5500

Standard Form 298 (Rev. 2-89)
Prescribed by ANSI Std. Z39-18
298-102